

This is an Open Access document downloaded from ORCA, Cardiff University's institutional repository: <https://orca.cardiff.ac.uk/id/eprint/144073/>

This is the author's version of a work that was submitted to / accepted for publication.

Citation for final published version:

Han, Quanquan, Low, Kenny W.Q., Gu, Yuchen, Wang, Xiaobo, Wang, Liqiao, Song, Bo, Huang, Chuanzhen and Setchi, Rossitza 2021. The dynamics of reinforced particle migration in laser powder bed fusion of Ni-based composite. Powder Technology 394 , pp. 714-723. 10.1016/j.powtec.2021.09.005

Publishers page: <http://dx.doi.org/10.1016/j.powtec.2021.09.005>

Please note:

Changes made as a result of publishing processes such as copy-editing, formatting and page numbers may not be reflected in this version. For the definitive version of this publication, please refer to the published source. You are advised to consult the publisher's version if you wish to cite this paper.

This version is being made available in accordance with publisher policies. See <http://orca.cf.ac.uk/policies.html> for usage policies. Copyright and moral rights for publications made available in ORCA are retained by the copyright holders.



The dynamics of reinforced particle migration in laser powder bed fusion of Ni-based composite

Quanquan Han^{a*}, Kenny W.Q. Low^b, Yuchen Gu^b, Xiaobo Wang^c, Liqiao Wang^{a*}, Bo Song^c, Chuanzhen Huang^a, Rossitza Setchi^d

^aKey Laboratory of High Efficiency and Clean Mechanical Manufacture of Ministry of Education, Key National Demonstration Center for Experimental Mechanical Engineering Education, School of Mechanical Engineering, Shandong University, Jinan, 250061, China

^bCollege of Engineering, Swansea University, Swansea, SA1 8EN, UK

^cState Key Laboratory of Materials Processing and Die & Mould Technology, Huazhong University of Science and Technology, Wuhan, 430074, China

^dCardiff School of Engineering, Cardiff University, Cardiff, CF24 3AA, UK

Corresponding author:

Quanquan Han, hanquanquan@sdu.edu.cn, +86531-88392608

Liqiao Wang, wangliqiao@sdu.edu.cn

Abstract

The dynamics of the reinforced particles' migration remains unclear during the rapid non-equilibrium laser powder bed fusion (LPBF) process. Conducting real-time observations to obtain a comprehensive understanding of the reinforcements' movement is challenging due to the complex physical phenomena that occur during experimentation. The proposed numerical simulation in the present study incorporates a Lagrangian discrete phase model (DPM) to simulate the added submicrometre-sized TiC particles. The simulation results indicate that the migration of TiC particles was primarily induced by the combination of recoil pressure and Marangoni convection force. The TiC particles were also noted to be relatively uniformly distributed in the LPBF-fabricated Hastelloy X-1 wt.% TiC composite under a 600 mm/s scanning speed. The present study offers insights into understanding the dynamics of added reinforced phases within the LPBF additive-manufacturing process to further accelerate the development of advanced metal matrix composites processed using the LPBF process.

Keywords

Laser powder bed fusion; Ni-based composite; Hastelloy X; numerical simulation; particles migration

1. Introduction

Ni-based composites exhibit exceptional high-temperature properties as well as oxidation and corrosion resistance. Because of these qualities, these materials are widely used in the aerospace and power industries, such as in combustion cans, transition ducts and flame holders [1][2]. These engineering components generally have complex geometries, so the topology optimisation method is often used to optimise their geometry to further improve their performance. Considering these complex geometries, traditional manufacturing processes such as machining and casting are incapable of manufacturing these high-performance Ni-based composites [3][4].

Laser powder bed fusion (LPBF) is an advanced manufacturing process in which a high-power laser is used to melt and fuse powders layer by layer to form three-dimensional components [5][6][7]. Because LPBF offers the capability to manufacture high-performance complex-shaped components, the technology is widely used to manufacture advanced **metal matrix** composites (MMCs). For instance, Gao et al. [8] investigated the microstructural, interfacial and mechanical performance of LPBF fabricated TiN nanoparticle reinforced AlSi10Mg composite; they have found that the composite powder offered a superb processability due to the enhanced laser absorptivity induced by the reinforced TiN phase. Nano-scaled TiN particles were detected to be evenly distributed while a few agglomerated TiN particles gathered to form clusters. Han et al. [9] studied the tensile behaviour of LPBF-fabricated (TiB+TiC)/Ti composites where the TiB+TiC reinforced phase was formed via the in-situ chemical reaction between Ti and B₄C materials. The authors noted that a rise in B₄C content led to a decrease in the relative density of the fabricated composites due to the formation of macro-cracks. The dispersion and grain refinement strengthening mechanisms were found to be the primary strengthening mechanism in this composite, while the formed cracks induced

by the B₄C clusters degraded the mechanical performance. Yang et al. [10] investigated the degradation behaviour of bioglass-reinforced Mg-based composite and the authors found that refined grains together with orderly dispersed reinforcing particles contributed to the enhanced mechanical properties. Also, the incorporated bioglass promoted the apatite deposition on the Mg matrix.

In addition to the successful exploration on LPBF of Al, Ti and Mg-based composites, recent studies have focussed on LPBF of advanced Ni-based composites. For example, Zhang et al. [11] investigated the tensile and creep properties of WC-reinforced Ni-based composites fabricated by LPBF process; they have demonstrated that the fabricated composites exhibited lowest stress concentration under the optimal volumetric energy density. The grain refinement, however, contributed to a reduction in creep life and ductility with increasing the energy density value. Han et al. [12] examined the effects of TiC content on microstructure and mechanical properties of Ni-based nanocomposites manufactured by LPBF and found that the added 1 wt.% TiC nanoparticles led to 19% and 10% improvements in tensile strength and elongation, respectively, although a further increase in TiC content to 3 wt.% resulted in a 10% loss in elongation at room temperature condition.

The above studies mainly focused on the effects of reinforcement on the microstructure and mechanical performance of MMCs through experimental investigations. These studies also revealed that the migration of added reinforced particles was strongly connected to the components' mechanical performance [13]. Conducting real-time observations to obtain a comprehensive understanding of the reinforcements' movement is challenging, however, due to the complex physical phenomena that occur during experimentation.

As an alternative, numerical simulations offer researchers the ability to investigate complicated laser-material interactions at different scales to reveal melt pool development, the defects-formation mechanism and other phenomena during the LPBF of single materials [14][15][16]. For instance, Lu et al. revealed microstructure development by coupling thermal fluid dynamics

and microstructure analysis using phase field modelling [17]. Khairallah et al. developed multi-physics computational fluid dynamics models within the single-track/single-layer melting process to simulate the effects of recoil pressure and Marangoni convection on melt pool evolution, pores and spatter formation [14]. Manvatkar et al. studied heat transfer and material flow during the multi-layer LPBF process through the development of transient, heat-transfer and fluid-flow models [18]. Bayat et al., who developed a multi-physics model to investigate 'lack of fusion' voids and evolution within the LPBF of multi-track/multi-layer processes, noted a lack of fusion defects mostly in the lower layers, where the thermal energy of the fluid is typically lower than in higher levels [19]. Zhang et al. revealed the dynamic characteristics of melt pools during the LPBF of titanium alloys via multi-physics simulation by considering phase transitions, recoil pressure, surface tension and Marangoni convection [20].

In addition to these numerical studies of the LPBF of single materials, a few investigations have reported the successful implementation of numerical simulations on the LPBF of multi-materials. Shinjo and Panwisawas developed a high-fidelity thermal-solutal-fluid modelling approach to investigate the physical link between metal vapour mass loss and the melt flow process during the LPBF of 21 transition metals and 3 binary alloys. Their findings offer a novel pathway to understanding the complex interdependent thermal-fluid flow dynamics and have contributed to digital materials design [21]. Gu et al. developed an integrated multi-physics modelling framework to reveal the melt pool evolution and track morphology of multiple materials deposited on multilayers [22]. They employed the discrete element method to produce the powder deposition process of multiple materials in different patterns. Their findings provide valuable insights into the design and optimisation of multi-material additive-manufacturing processes. **More recently, Yang et al. [23] proposed a simulation scheme to trace the migration and interactions of nanoparticles in the melt pool by adopting heat-melt-microstructure-coupled phase-field simulation with nanoparticle kinematics. Van der Waals attraction and electrostatic repulsion were considered during the numerical simulation; they have demonstrated that the melt-flow-driven**

effect (Marangoni force) dominated the nanoparticles migration and interaction provided the nanoparticles were sufficiently spaced. Their study demonstrates the significant potential of employing simulation methodology to optimise the LPBF process in order to minimize the agglomeration effects within LPBF of advanced MMCs.

In conclusion, several researchers have investigated microstructures and mechanical performance during the LPBF of advanced Ni-based composites, often using the multi-physics modelling method to understand the complex physics involved in the LPBF of single and multiple materials. To the best of our knowledge, however, reinforcement phases have not been incorporated in the **numerical simulation of flow field** within the LPBF of metal matrix composites to understand their migration behaviour during the complex laser-material interaction. In this context, we developed a multi-phase model that incorporates a Lagrangian discrete phase model (DPM) to investigate the dynamics of submicrometre-sized TiC particle migration during the LPBF of Hastelloy X-TiC composites. We validated the simulation results by inspecting melt pool development and TiC particle distribution following the LPBF process.

2. Numerical model

2.1. Governing equations

The LPBF additive-manufacturing (AM) simulation was performed on the basis of mass, momentum and energy conservation equations for incompressible Newtonian fluid, which may be expressed as [24][25]:

Mass

$$\nabla \cdot \vec{v} = 0 \quad (1)$$

Momentum:

$$\frac{\partial}{\partial t}(\rho \vec{v}) + \nabla \cdot (\rho \vec{v} \vec{v}) = -\nabla P + \rho \vec{g} + k' \gamma \vec{n} + \nabla_s \gamma \quad (2)$$

Energy:

$$\rho c_p \left(\frac{\partial T}{\partial t} + \vec{v} \cdot \nabla T \right) = \nabla \cdot (k \nabla T) + S_h \quad (3)$$

where \vec{v} is the velocity vector of fluid; ρ , P and $\rho\vec{g}$ denote the density, static pressure and gravitational body force, respectively. k' is the curvature of the interface, γ denotes the surface tension coefficient; \vec{n} and ∇_s represent the unit normal to the local surface and surface gradient operator. c_p and k represent the specific heat capacity and thermal conductivity, respectively; and S_h and T denote the energy source and temperature, respectively.

The volume of fluid (VOF) method was used to track the free surface of the molten pool. The fluid fraction (V_F) varied based on the advection equation, where $V_F = 0$ represents a void cell and $V_F = 1$ indicates a full cell. The VOF equation is expressed as:

$$\frac{\partial V_F}{\partial t} + \nabla \cdot (\vec{v}V_F) = 0 \quad (4)$$

The phase change between the solid and liquid phases was considered in modelling and the enthalpy-based continuum model is provided by:

$$h = c_p \cdot T + f(T) \cdot L_f \quad (5)$$

where L_f is the latent heat during phase transformation and $f(T)$ represents the volume fraction of solid/liquid interface with respect to temperature:

$$f(T) = \begin{cases} 0, & T \leq T_S \\ \frac{T-T_L}{T_L-T_S}, & T_S < T < T_L \\ 1, & T \geq T_L \end{cases} \quad (6)$$

where T_L and T_S represent the liquidus and solidus temperatures, respectively.

The surface tension (γ) is a function of temperature and may be shown as:

$$\gamma(T) = \gamma_m + \frac{d\gamma}{dT} \cdot \Delta T \quad (7)$$

where γ_m is the surface tension at the melting temperature while $\frac{d\gamma}{dT}$ and ΔT represent the surface tension gradient and temperature difference versus melting temperature, respectively.

2.2. Gaussian heat source and recoil pressure

The heat flux followed a Gaussian distribution and may be expressed as

[26]:

$$I(r) = \frac{2AP}{\pi r_0^2} \exp\left(-\frac{2r^2}{r_0^2}\right) \quad (8)$$

where A is absorptivity, P and r_0 are laser power and laser spot radius (respectively), and r denotes radial distance from the laser centre.

In general, the recoil pressure induced by the evaporation is the main driving force for keyhole formation and the migration of added reinforced particles; the recoil pressure (P_r) can be expressed as [27]:

$$P_r(T) = 0.54P_0 \cdot \exp\left(L_v \frac{T-T_b}{RTT_b}\right) \quad (9)$$

where P_0 and L_v denote the pressure of the surroundings and latent heat of evaporation, respectively, while R and T_b represent the universal gas constant and boiling temperature, respectively.

2.3. Discrete phase model

A Lagrangian DPM was used to simulate the TiC reinforcement particles. The fluid phase is treated as a continuum by solving the Navier-Stokes equations, while the dispersed phase was solved by tracking a large number of particles through the calculated flow field. The DPM follows the Ruler-Lagrange approach and the particle-particle interaction is negligible, particle temperature is assumed to be the same as the local temperature the fluid flow [28][29]. The DPM model was used to predict the trajectory of a discrete phase particle by integrating the force balance on the particle; this force balance may be written as [30]:

$$m_p \frac{d\vec{v}_p}{dt} = \vec{F}_D + \vec{F}_L + \vec{F}_G + \vec{F}_R \quad (10)$$

where \vec{v}_p denotes the particle velocity; F_D and \vec{F}_G represent the drag force and gravity force, respectively. \vec{F}_R is a rotation-induced additional force, which is an intrinsic part of the particle acceleration and \vec{F}_L is the Saffman's lift force.

The aerodynamic drag force on a particle is proportional to the phase slip

velocity, the difference between the fluid and particle velocities, the drag force \vec{F}_D can be expressed as [30]:

$$\vec{F}_D = \frac{1}{2} C_D \cdot \rho_f \cdot A_p \cdot |\vec{v} - \vec{v}_p| (\vec{v} - \vec{v}_p) \quad (11)$$

where ρ_f and A_p denote the fluid phase density and the area of the particle projected in the flow direction, respectively. C_D is the drag coefficient, which depends on the relative Reynolds number $Re_p = \frac{\rho_f |\vec{v} - \vec{v}_p| d_p}{\mu}$. The Saffman's lift force may be expressed as [31]:

$$\vec{F}_L = \frac{2K_1 v^{1/2} \rho d_{ij}}{\rho_p d_p (d_{lk} d_{kl})^{1/4}} (\vec{v} - \vec{v}_p) \quad (12)$$

where $K_1 = 2.594$ and d_{ij} is the deformation tensor. This option is recommended only for submicron particles [31].

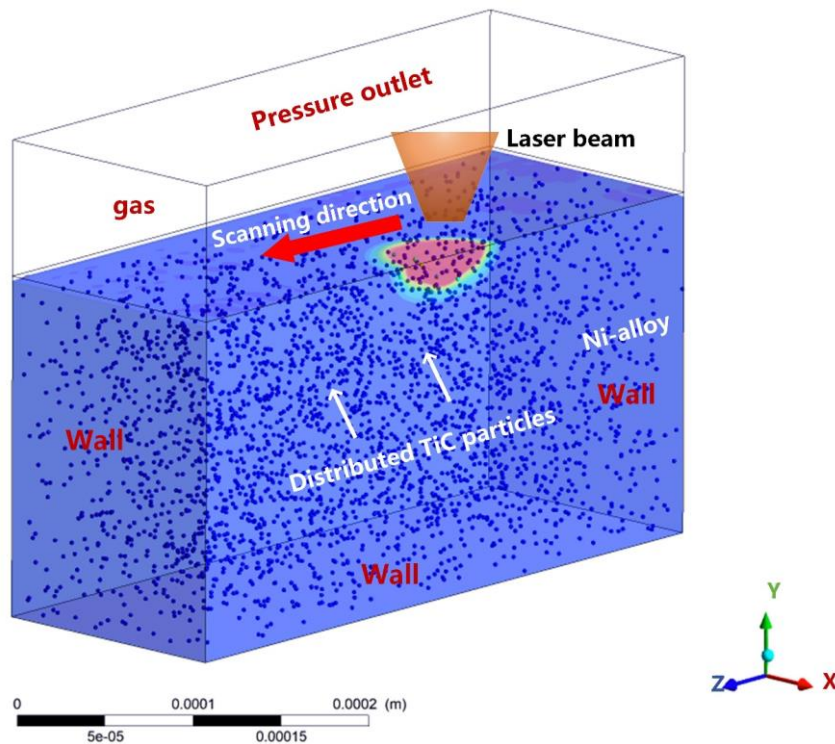


Fig. 1. Schematic of the simulation model.

Fig. 1 shows a schematic of the simulation model developed in the present study. ANSYS Fluent v19.2 was used to solve all the transport equations to implement the computational fluid dynamics model. The dimensions of the calculation domain were 400 x 150 x 280 μm , with 134,400 hexahedral cells with a uniform grid spacing of 5 μm . The length of the simulated single track

was set to 200 μm to study the dynamics of melt pool development and TiC particle migration. The TiC reinforcement particles were generated by the DPM with a uniform diameter of 200 nm and a total number of 3,000 to approximately simulate the added 1 wt.% TiC particles. The density and specific heat values of TiC were $4,930 \text{ Kg} \cdot \text{m}^{-3}$ and $544.25 \text{ J} \cdot \text{Kg}^{-1} \cdot \text{K}^{-1}$, respectively. Table 1 shows the physical properties of the Hastelloy X (HX) nickel alloy used in the study as well as various LPBF processing parameters. We should note that the surface tension, thermal conductivity, specific heat and dynamic viscosity properties were temperature dependent rather than being constant values.

Table 1. Physical properties of Hastelloy X (HX) alloy and LPBF processing parameters [20][32][33][34].

Property (unit)	Symbol	Value
Density ($\text{Kg} \cdot \text{m}^{-3}$)	ρ	8240
Solidus temperature (K)	T_s	1533
Liquidus temperature (K)	T_L	1628
Boiling temperature (K)	T_b	3100
Universal gas constant ($\text{J} \cdot \text{mol}^{-1} \cdot \text{K}^{-1}$)	R	8.3144
Ambient temperature (K)	T_a	300
Ambient pressure (Pa)	P_0	1.0×10^5
Surface tension ($\text{N} \cdot \text{m}^{-1}$)	γ	$1.88 - 0.0001 \cdot (T - 1580)$
Latent heat of fusion ($\text{J} \cdot \text{Kg}^{-1}$)	L_f	2.76×10^5
Latent heat of evaporation ($\text{J} \cdot \text{Kg}^{-1}$)	L_v	6.3×10^6
Radiation emissivity	ε	0.8
Laser power (W)	P	200
Laser radius (m)	r_0	3.5×10^{-5}
Scan speed (mm/s)	V	300, 600
Laser absorptivity	A	0.38
Thermal conductivity ($\text{W} \cdot \text{m}^{-1} \cdot \text{K}^{-1}$)	K	$\begin{cases} 0.019T + 4.6 & T \leq 1533 \\ -0.05T + 109.54 & 1533 < T \leq 1628 \\ 29 & T > 1628 \end{cases}$
Specific heat ($\text{J} \cdot \text{Kg}^{-1} \cdot \text{K}^{-1}$)	C_p	$\begin{cases} 0.22T + 373 & T \leq 1533 \\ -0.347T + 1242 & 1533 < T \leq 1628 \\ 677 & T > 1628 \end{cases}$
Dynamic viscosity ($\text{Kg} \cdot \text{m}^{-1} \cdot \text{s}^{-1}$)	μ	$\begin{cases} 0.243 \cdot e^{-0.0021 \cdot T} + 373 & T \leq 1533 \\ 0.0297 - 0.0000136 \cdot T & 1533 < T \leq 1628 \\ 0.00548 & T > 1628 \end{cases}$

2.4. Boundary conditions

The boundary conditions are illustrated in Fig. 1. As the figure shows, thermal conduction, convection and radiation were applied on the side and

bottom surfaces of the powder bed, defined as walls. The top and side surfaces of the gas phase were defined as pressure outlets, open to the ambient atmosphere. A laser was used to irradiate the vapour-liquid-free surface. The energy-balance equation may be expressed as:

$$k \cdot \frac{\partial T}{\partial n} = -h_c(T - T_{am}) - k\varepsilon(T^4 - T_{am}^4) \quad (13)$$

where k and ε donate the Boltzmann constant (5.67×10^{-8}) and radiation emissivity, respectively. h_c is the heat convection coefficient and T_{am} represents the ambient temperature (300 K).

3. Experimental procedures

A Renishaw AM250 machine equipped with a modulated ytterbium-fibre laser was employed in this work to manufacture the HX-1 wt.% TiC composite specimens. LPBF process parameters optimisation was investigated through the indicator: laser energy density ($\sigma = \frac{P}{V \cdot l \cdot h}$), where P and V represent the laser power and scanning speed; l and h denote the powder layer thickness and hatch spacing, respectively [35]. The optimum laser energy density to manufacture nearly fully dense HX-1 wt.% TiC composite specimens was determined to 83.3 J/mm^3 ($P = 200 \text{ W}$, $h = 100 \text{ }\mu\text{m}$, $l = 40 \text{ }\mu\text{m}$ and $v = 600 \text{ mm/s}$). This optimal parameter combination was employed to manufacture the validation specimens in the current study. Laser scanning speeds of both 600 mm/s and 300 mm/s were studied in the numerical modelling in the present study to examine the effects of process parameters on the dynamics of reinforced particle migration.

The raw gas-atomised HX powder used in this work was supplied by Sandvik Osprey (Neath, UK), with an average particle size of $32.5 \text{ }\mu\text{m}$. The TiC particles ($< 200 \text{ nm}$) were obtained from Sigma Aldrich (UK). Both the HX powder and 1 wt.% TiC particles were mixed using a high-speed mixer to disperse the TiC particles amongst the HX powder. The typical mixing

parameters included a mixing speed = 1200 rpm and mixing time = 5 minutes [36]. Fig. 2 shows the mixed HX-1 wt.% TiC composite powder feedstock, where the submicrometre-sized TiC particles were uniformly coated on the HX powder. Note that, since the TiC particles were uniformly distributed amongst the HX powder, it was thus reasonable in the numerical modelling to use the DPM model to generate evenly distributed TiC particles in the HX matrix to investigate the dynamics of their migration, as indicated in Fig. 1.

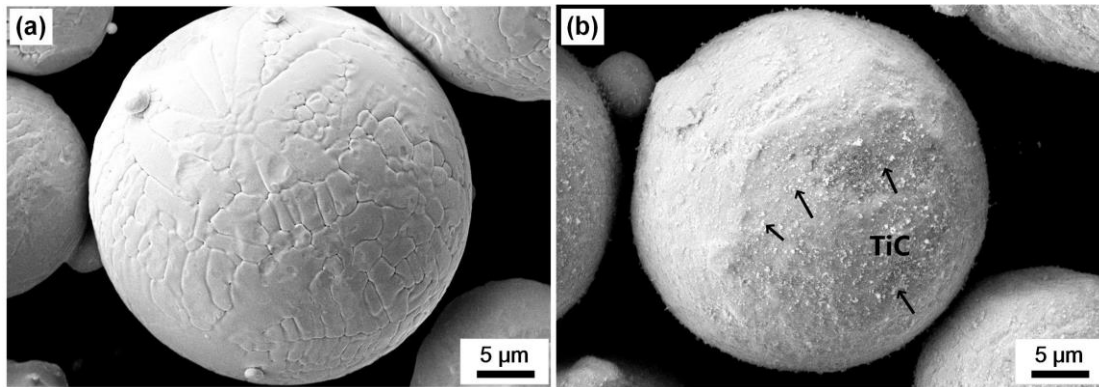


Fig. 2. The raw materials used for this study: (a) pure Hastelloy X (HX), (b) the HX-1 wt.% TiC composite powder feedstock.

4. Results and discussion

4.1. Single-track simulation

Fig. 3 shows the melt pool evolution and TiC particle migration during single-track melting under a scanning speed of 600 mm/s. **In the present simulation, the powder bed was simulated using a bulk calculation domain (400 x 150 x 280 μm) rather than using discrete powders. Since the experimental results indicated that the added sub-micrometre TiC particles were uniformly coated on the surface of HX powders, the assumption used is that the TiC particles were uniformly dispersed in the HX matrix before the laser melting, and the aim of the numerical simulation is to investigate the TiC particles migration behaviour during the single-track laser melting process.** The length of the scanned single track was set at 200 μm, with a determined **total** scanning time of 333 μs. Overall, the melt pools captured were found to exhibit a nearly

semi-ellipse-shaped geometry, but both the width and depth of the melt pools gradually increased with continued laser scan irradiation. This situation could be explained by the fact that the solidified zone exhibited higher effective thermal conductivity compared to the loose powder bed. In other words, the fused material conducted heat much better than the unmelted powder did. Another contributor that caused the melt pool shape change to some extent at different times was the interactive forces, including recoil pressure, surface tension and Marangoni convection [19][32].

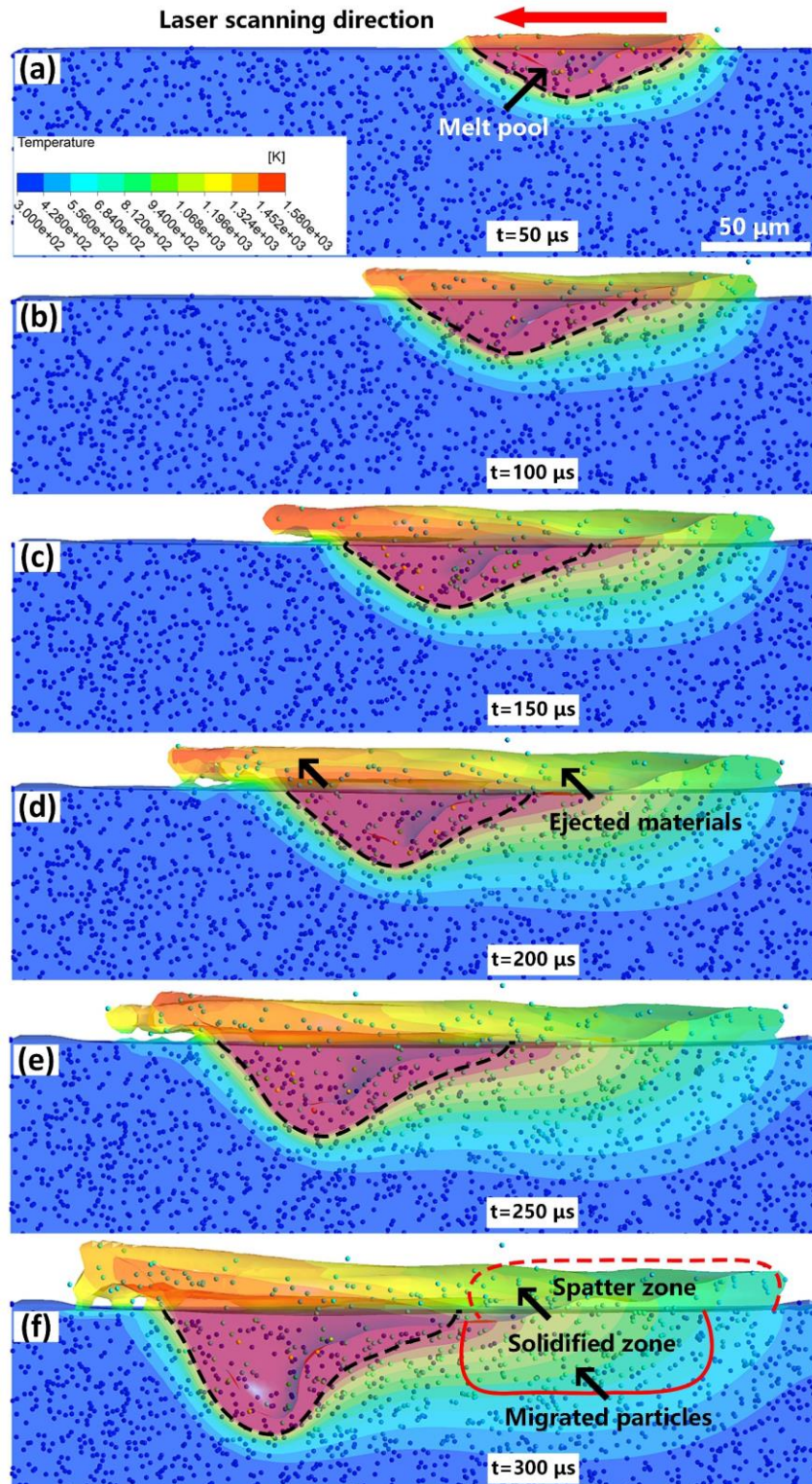


Fig. 3. Cross-sectional view of melt pool evolution during single-track scanning under a scanning speed of 600 mm/s at different locations, **the indicated time is an instant time**: (a) $t=50 \mu\text{s}$, (b) $t=100 \mu\text{s}$, (c) $t=150 \mu\text{s}$, (d) $t=200 \mu\text{s}$, (e) $t=250 \mu\text{s}$ (f) $t=300 \mu\text{s}$.

The simulation results demonstrated that partial molten HX material was ejected from the melt pools. This phenomenon was found to be more obvious when the laser scanning time was over 100 μs . The molten material was

ejected because the laser-material interaction caused a strong energy input. Strong evaporation occurred when the melt pool temperature was greater than the boiling temperature of the main alloying elements and the HX alloy, and the induced recoil pressure may have pushed the deformable liquid down and made a depression zone, or hole [37]. The keyhole size increased with further increase in temperature due to greater recoil pressure. In general, when the recoil pressure surpasses a certain threshold, the molten material may be pushed out of the melt pools to form a spatter zone [14][38]. Note that a few added TiC particles moved to the spatter zone (Fig. 3f), while the rest were still evenly distributed in the melt pools. Considering the Gaussian distribution of the laser source that was employed, a significant thermal gradient existed at the laser-material interaction zone, suggesting that the central zone of the melt pools had a much higher temperature compared to the melt pool edge zones. Since the surface tension was temperature dependent, the fluid in the melt pools was driven to move by Marangoni convection [39][40][41].

Therefore, in addition to the recoil pressure causing the TiC particles to migrate, the Marangoni convection force was another significant contributor to the movement of the TiC particles, which were uniformly distributed in the melt pools. When the laser scanning time was set to 300 μs (Fig. 3f), the melt pool exhibited a keyhole-shaped geometry that differed from that of the captured melt pools shown in Fig. 3a-e. Also, the migrated TiC particles were found to be uniformly distributed in the solidified zone during the single-track simulation. The migration of these TiC particles was considered to have been primarily caused by the Marangoni convection force in the melt pools, while the ejected TiC particles distributed in the spatter zone were mainly driven by the recoil pressure.

The fluid velocity magnitude in the melt pools at different time moments was captured (Fig. 4) to demonstrate the effects of Marangoni convection and

recoil pressure on TiC particles' migration when the laser scanning speed was fixed at 600 mm/s. The fluid velocity magnitude varied at the four typical moments (50, 100, 200 and 300 μ s), which was primarily caused by the combination of recoil pressure and Marangoni convection. When the scanning was continued from 50 to 300 μ s, the captured maximum velocity in the melt pools exhibited an incremental trend, but the maximum velocity at $t = 300 \mu$ s was found to be 3.964 m/s, which was lower than the case at $t = 200 \mu$ s, where a 5.234 m/s fluid velocity was captured.

Considering the melt pool development within the single-track melting, the heat input accumulated such that the solidified zone exhibited higher thermal conductivity, thus enabling the melt pools to grow larger with continued laser scanning. In particular, a keyhole-shaped melt pool was captured at $t = 300 \mu$ s, since the recoil pressure tended to be dominant. This finding indicated that the melt pool tended to be unstable with increased scanning times during single-track melting, which may have been attributable to the recoil pressure. This question was confirmed by the fluid velocity magnitude that was captured, where the melt pool had a smaller maximum fluid velocity (3.964 m/s) at $t = 300 \mu$ s compared to $t = 200 \mu$ s (Fig. 4c-d). Note that at the scanning moments we captured, more melt liquids tended to flow to the rear of the melt pools (opposite the laser scanning direction), suggesting that more TiC particles might have moved to the rear of the melt pools.

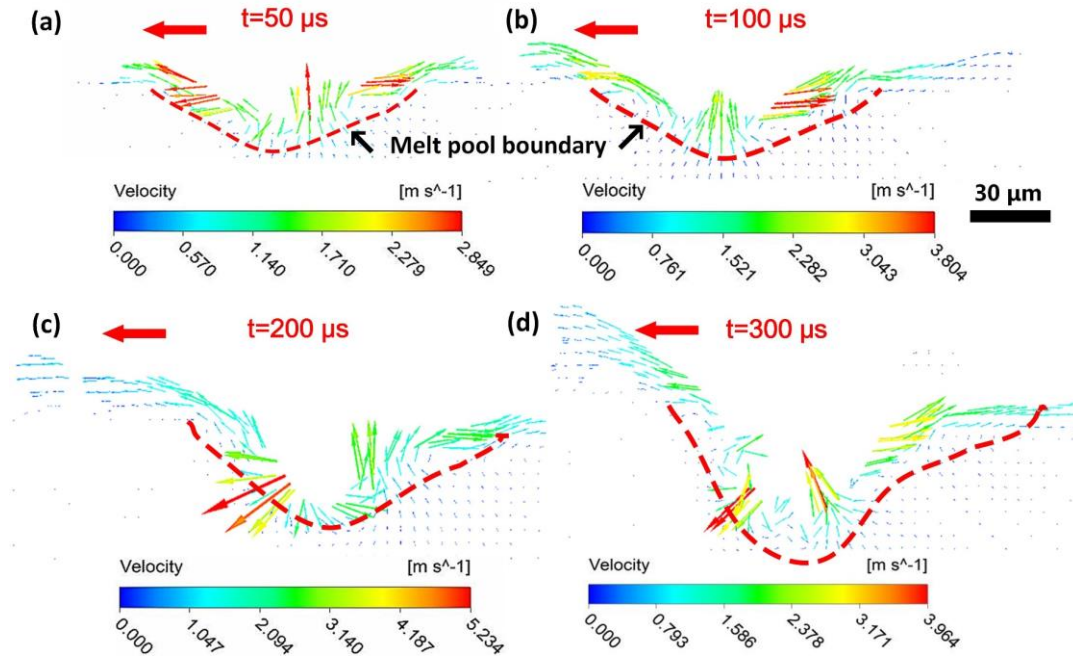


Fig. 4. The fluid velocity magnitude in the melt pool at (a) $t=50 \mu\text{s}$, (b) $t=100 \mu\text{s}$, (c) $t=200 \mu\text{s}$ and (d) $t=300 \mu\text{s}$ (the red arrow indicating the laser scanning direction).

Fig. 5 shows the maximum temperature and fluid velocity distribution captured at different laser scanning moments under a 600 mm/s scanning speed. This information was useful to further understand the dynamics of the TiC particles' migration in the melt pools. As the figure shows, the maximum temperature captured remained greater than the boiling temperature of HX ever since the start of the single-track melting. Because the laser beam used in the study followed a Gaussian distribution, the zone with the highest temperature was generally a very small area, located in the middle of the melt pools. The maximum melt pool temperature showed an overall increase with continued laser scanning until the single-track melting was complete due to the stored energy gained from scanning the solidified portion of the single track. Previous studies have reported the heat accumulation from scanned tracks/layers within the LPBF process, resulting in an increase in both overall and maximum temperatures [42][43].

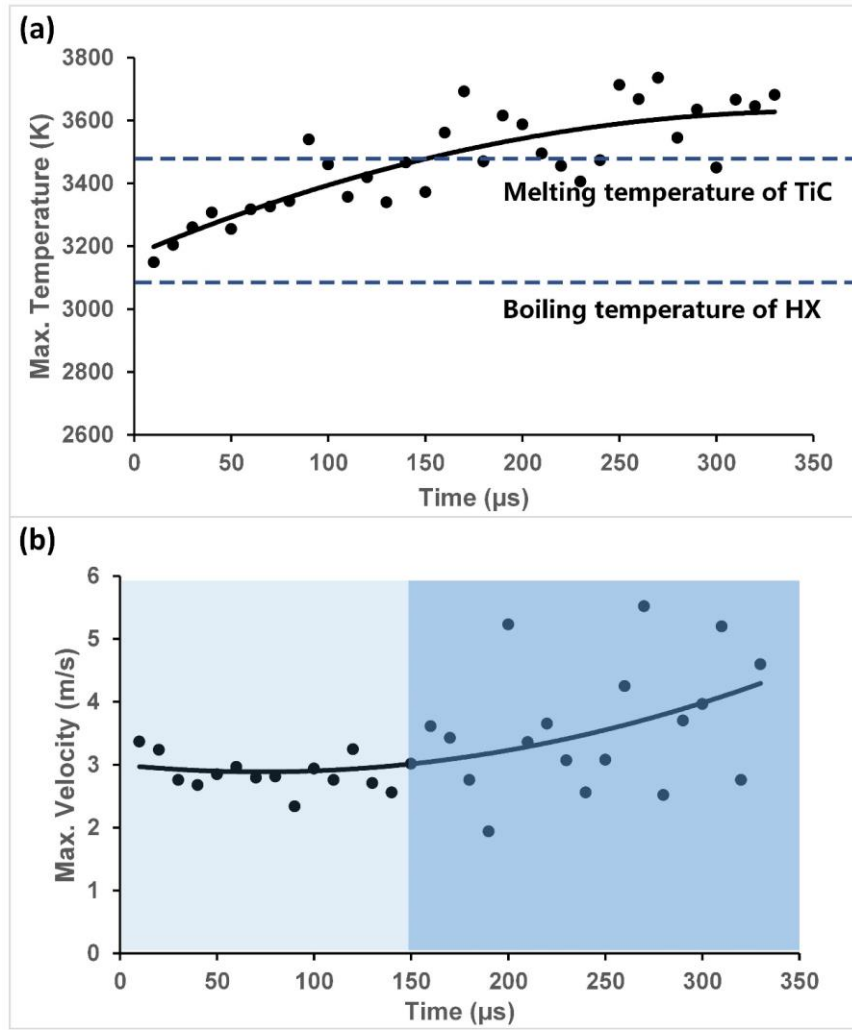


Fig. 5. The maximum temperature captured (a) and fluid velocity (b) in the melt pools during single-track melting.

In terms of the maximum temperatures captured in the study, the temperature fluctuation seemed to be more obvious when the laser scanning time was over 100 μs , although the maximum temperature exhibited an overall incremental trend. This situation may be explained by the unstable melt pools that formed due to strong evaporation. With continued laser irradiation, the zone of melt pools with a temperature greater than the boiling temperature of HX (3100°C) became larger, thus leading to more significant evaporation and recoil pressure. Note that the maximum temperature that was captured was greater than the melting temperature of TiC when a laser scanning time of $t > 150$ μs was used, even though this kind of zone in the melt pool was fairly small. This finding indicates that during the LPBF of HX-

TiC composite, a limited number of TiC particles may be melted and then resolidify.

Likewise, the maximum fluid velocity captured in the study was also found to have increased during the single-track melting (Fig. 5b). As discussed above, the fluid velocity magnitude captured was determined by the combination of recoil pressure and Marangoni convection. Interestingly, fluctuations in maximum velocity tended to be more apparent when the laser irradiating time was beyond 150 μs , thus indicating that the melt pools that had formed became unstable once recoil pressure became predominant. The maximum velocity captured showed agreement with the maximum temperature in terms of fluctuation magnitude, which suggests that evaporation played a significant role in determining the melt pools' stability. The recoil pressure could have migrated the molten metal and TiC particles to form spatters along the single track. The TiC particles that migrated might have formed clusters, which would have been detrimental to the surface quality and the melting process for subsequent layers.

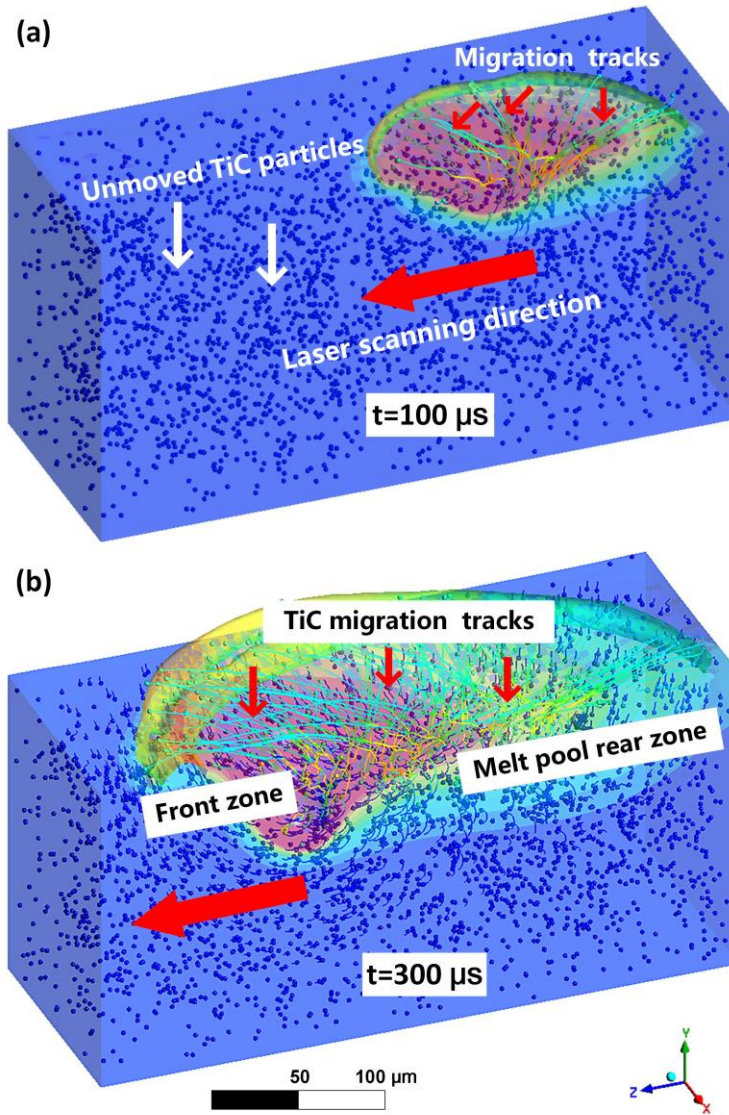


Fig. 6. The TiC particles' captured migration tracks at **instant times**: (a) $t = 100 \mu\text{s}$ and (b) $t = 300 \mu\text{s}$.

Fig. 6 shows typical TiC particle migration behaviours at $t = 100 \mu\text{s}$ and $300 \mu\text{s}$, with a laser scanning speed fixed at 600 mm/s . The TiC particles' migration path was tracked to clearly demonstrate their migration behaviour. Since the dynamic viscosity of the melted HX material played a significant role in the migration of TiC particles in the melt pools, the dynamic viscosity was set to be temperature dependent in the present modelling (Table 1) to more precisely approximate the practical LPBF process. A very limited number of TiC particles were noted to have migrated from the centre to the edge of the melt pool when the laser irradiation was set at $t = 100 \mu\text{s}$ (Fig. 6a). Note that

the remainder of the TiC particles were kept unmoved in the simulation domain because the HX matrix was still in the solid state, and the HX was set to have a very high viscosity coefficient. When the laser melting was continued to $t = 300 \mu\text{s}$, a large number of TiC particles were driven to migrate to the spatter zone, particularly to the melt pool's rear zone (Fig. 6b), also known as the low-pressure zone, as strong pressure formed on the melting front (Bayat, Mohanty and Hattel 2019). The interaction of a high-pressure zone in front of the melt pool and a low-pressure one at its rear enabled a local pressure gradient that functioned as a driving force to migrate the TiC particles to the rear zone.

The TiC particles' migration distance was much longer compared to the case at $t = 100 \mu\text{s}$. The melt pool size was larger at $t = 300 \mu\text{s}$, and the combination of recoil pressure and Marangoni convection force enabled a stronger driving force to migrate more TiC particles longer distances.

The migrated TiC particles were not found to have been agglomerated in the melt pools or the spatter zone during the single-track melting simulation. A previous study [43] revealed that the cooling rate decreases as the subsequent layers become deposited, which results in coarser solidified grains in the upper parts. This finding suggests that the dynamics of TiC particle migration may be more complicated during multi-layer simulation. Future work will be required to further investigate TiC particles' migration behaviour during multi-layer simulation within the LPBF process.

Fig. 7 shows the TiC particles' migration behaviour during single-track melting under two different laser scanning speed values. Both the fluid velocity and tracks of the migrated TiC particles are shown. The distance between points P_1 and P_2 was set to $200 \mu\text{m}$, which was the length of the simulated single track. The P_0 position, which was $120 \mu\text{m}$ away from the scanning start point P_1 , was used to investigate the effects of scanning speed on TiC particles' migration behaviour. The laser running time at P_0 was $t = 200$

μs when a 600 mm/s laser scanning speed was employed (Fig. 7a), while the laser running time was 400 μs when a speed value of 300 mm/s was used (Fig. 7b). The 300 mm/s laser scanning speed generated a much larger melt pool in terms of both depth and width compared to the 600 mm/s case, whereas a typical keyhole conduction mode was observed in the former case. In general, a deep and wide melt pool indicates that more laser rays have collided with the walls of the hole, leading to more energy being absorbed by the material as well as an increase in local temperature and recoil pressure. Indeed, based on the fluid flow behaviour, the 300 mm/s laser scanning speed induced much stronger recoil pressure and Marangoni convection force: the maximum fluid speed was detected to be 6.633 m/s compared to a value of 5.234 m/s for the 600 mm/s value. Note that, several TiC particles, which were enough distancing from the melt pool boundary, still show a rotative trajectory. This may be explained by the defined dynamic viscosity, which was set to temperature dependent and the data used were from previous studies (Table 1). Generally, the TiC particles in the unmelted zone did not move, so that no apparent rotative trajectory generated. The parameters used in determining the dynamic viscosity need to be further adjusted to improve the simulation's reliability in the future studies.

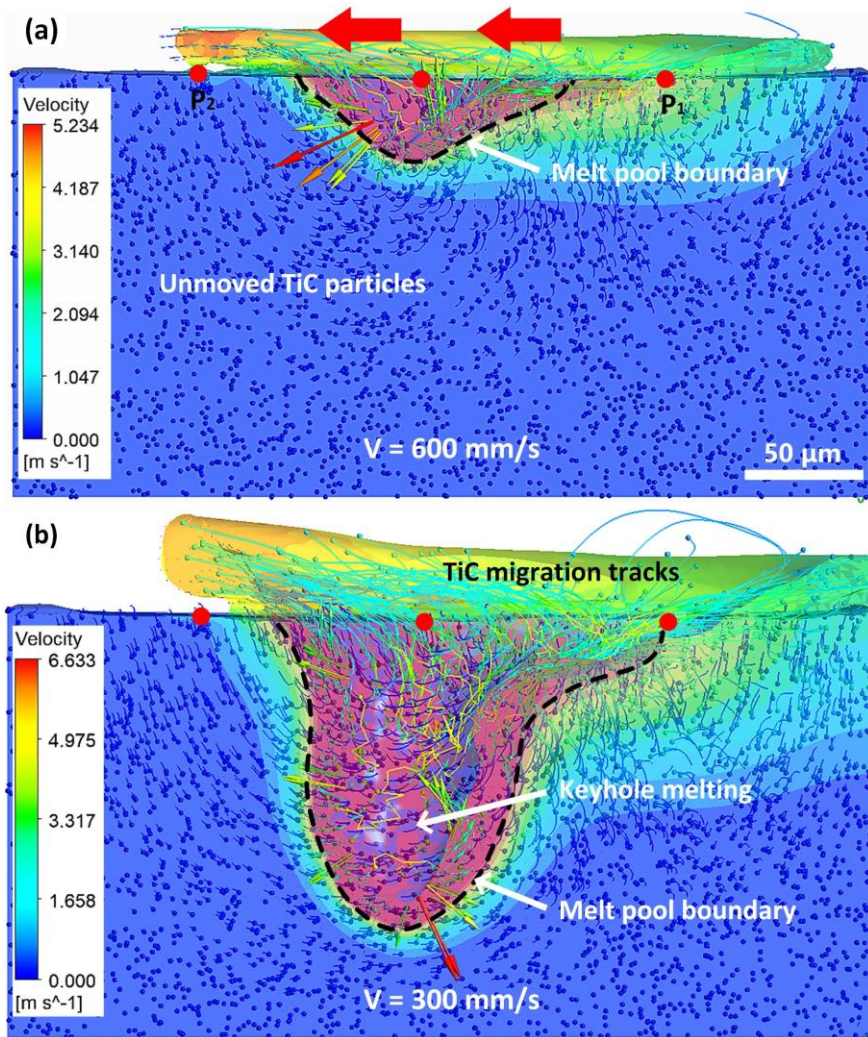


Fig. 7. The TiC particles migration behaviour under different laser scanning speeds: (a) 600 mm/s and (b) 300 mm/s.

4.2. Experimental validation

The LPBF process is known to be a complex multi-disciplinary laser-material interaction process. Numerical simulations of this process still require more effort to understand and reveal the multi-physics mechanisms involved. The following experimental study was conducted to validate the effects of laser scanning speed on melt pool development and TiC particle migration behaviour. Fig. 8 shows the microstructure of the fabricated HX-1 wt.% TiC composite specimen under different laser scanning speeds of 300 mm/s and 600 mm/s. The specimen was vertically sectioned (parallel to the build direction) and etched to reveal the melt pool boundaries, as indicated by the solid red lines.

As the figure shows, fairly uniform melt pools formed and few apparent defects were observed when a 600 mm/s laser scanning speed was employed. In contrast, the 300 mm/s laser scanning speed induced deeper melt pools, and a few typical keyhole pores formed at the bottom of the melt pools. The pores were found to have an average size greater than 30 μm . In terms of the melt pools, the experimental findings indicate that the laser scanning speed plays an important role in melt pool geometry. The composite specimen was chemically etched to reveal the melt pools, such that the migrated TiC particles were not observed in optical microscopy images under either laser scanning speed. We expected the TiC particles' migration behaviour to be different, however, since the melt pools had changed significantly.

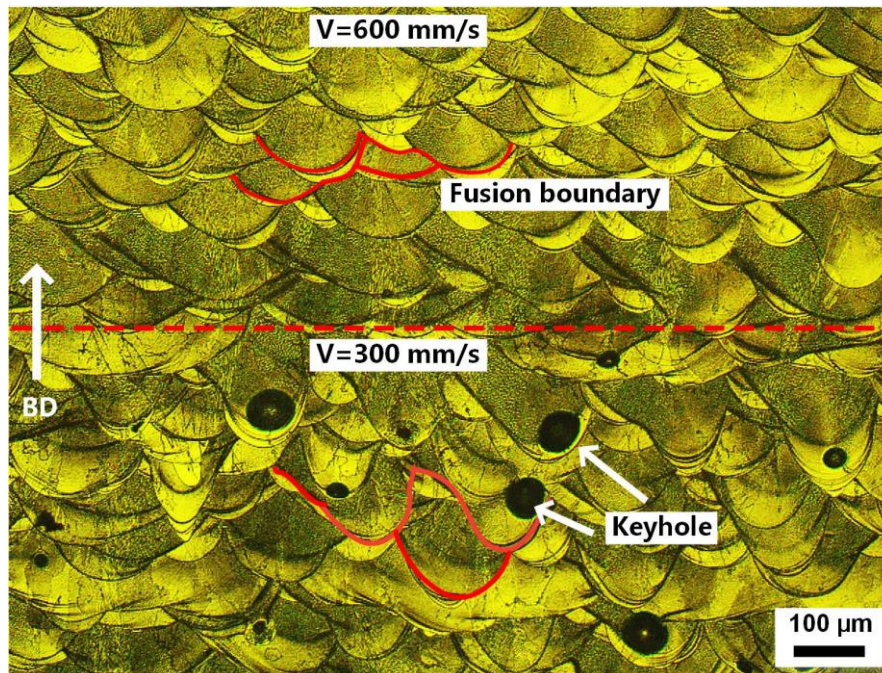


Fig. 8. Optical microscopy images of fabricated HX-1 wt.% TiC composite under different laser scanning speeds.

Fig. 9 shows backscattered electron (BSE) images of the LPBF-fabricated composite specimen under the optimal laser scanning speed of 600 mm/s. Typical columnar dendritic structures were noted to have formed along the build direction (Fig. 9a). The columnar grains tended to grow across a couple

of layers; a 40 μm layer thickness was used in the present study. The tiny black points with a size of ~ 150 nm were confirmed to be TiC particles (Fig. 9c-d), based on energy-dispersive X-ray spectroscopy analysis. The horizontal section (perpendicular to the build direction) was also inspected to examine the TiC particles' spatial distribution (Fig. 9b). We noted that the TiC particles were relatively uniformly distributed in the HX matrix after their migration in terms of both vertical and horizontal sections examination, although a very limited number of TiC clusters were also observed (marked in Fig. 9a). Based on the BSE inspection, the TiC particles around the fusion boundaries did not seem to be evenly distributed compared to other areas. This finding might be related to the remelting process, since the underlying solidified-layer was partially remelted to create a strong metallurgic bonding when a new powder layer was fused. The migrated TiC particles could be redistributed and moved under the combination of recoil pressure, Marangoni force and pressure gradient. Future work will be required to conduct multi-layer numerical simulation on the dynamics of TiC particles migration and employ high-resolution nano-computerized tomography (CT) scanning to investigate the spatial distribution of TiC particles in the HX matrix.

The experimental results showed consistency with the simulation: laser scanning speed played a significant role in melt pool development. The combination of recoil pressure and Marangoni convection force led to the migration of TiC particles and enabled a relatively uniform distribution of the particles within the HX matrix. The composite specimen under the 300 mm/s laser scanning speed (not shown in this paper) exhibited similar solidification structures compared to the 600 mm/s. The majority of the TiC particles were uniformly distributed in the HX matrix, but more TiC clusters were detected due to the instability of the melt pools.

We should note that the simulation in the present study only examined TiC particle migration during the single-track melting process. Future work will be

required to conduct multi-layer simulations to investigate the dynamics of TiC particle migration and to connect their distribution to the properties of LPBF-fabricated components.

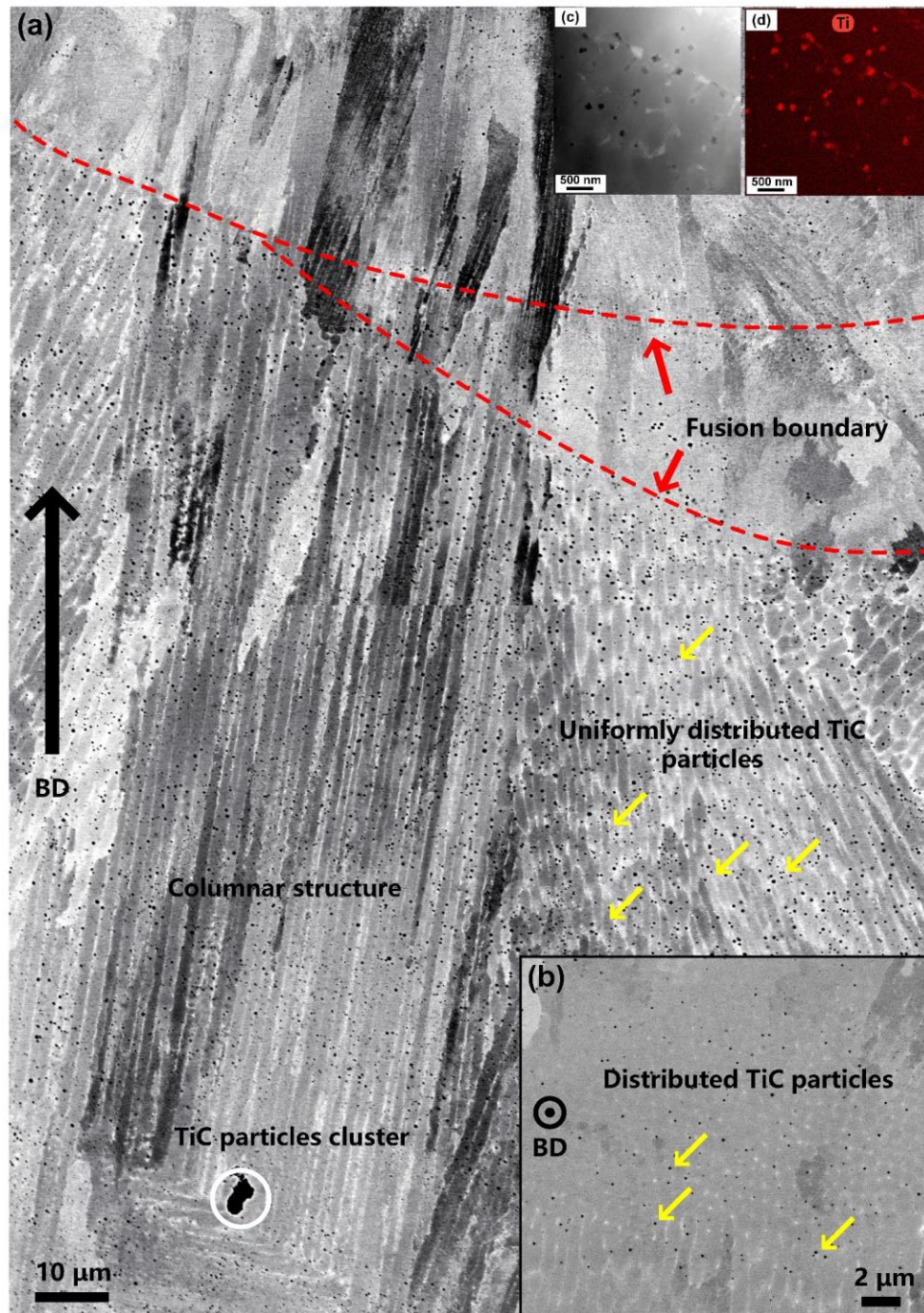


Fig. 9. Scanning electron microscopy images of the composite specimen showing the migration of TiC particles: (a) vertical section, (b) horizontal section, (c)-(d) EDX mapping zone from (a); the red arrows indicate the fusion boundaries, and the yellow arrows indicate the uniformly distributed TiC particles.

5. Conclusions

This study has investigated the dynamics of TiC particle migration in the laser powder bed fusion (LPBF) of Hastelloy X (HX) composites through both numerical and experimental methods. The following findings were derived from the present study.

- (1) The submicrometre-sized TiC particles (< 200 nm) were simulated by introducing a Lagrangian discrete phase model (DPM). The simulated TiC particles were set to be uniformly distributed in the HX matrix prior to single-track simulation. This uniform distribution was validated by using a high-speed mixing process, where we noted that the TiC particles were uniformly coated on the surface of the HX powder.
- (2) The migration of TiC particles was induced by the combination of recoil pressure and Marangoni convection force. With continued laser scanning, the recoil pressure tended to be dominant, leading to the formation of unstable melt pools and the ejection of TiC particles to the spatter zone.
- (3) As noted in the simulation, laser scanning speed played a significant role in the development of melt pools and the migration of TiC particles. The experimental results validated the simulation: a 600 mm/s scanning speed enabled consistent and uniform melt pool formation, while a 300 mm/s condition generated melt pools with apparent keyhole-pore defects. The TiC particles were also noted to be relatively uniformly distributed in the LPBF-fabricated HX-1% TiC composite under a scanning speed of 600 mm/s.

Our findings demonstrate that under the combination of recoil pressure and Marangoni convection force, part of the TiC particles migrated in the melt pools, and the remainder moved to the spatter zone during single-track simulation. The TiC particles that had migrated were detected to be uniformly distributed after rapid solidification had occurred, based on single-track

simulation. Multi-layer numerical simulation will be conducted in future work to investigate the dynamics of TiC particle migration and to examine the mechanical properties of LPBF-fabricated composites. The present study offers insights into understanding the dynamics of added reinforced phases within the LPBF additive-manufacturing process.

Acknowledgements

This work was supported by the National Natural Science Foundation of China (Grant No. 52005295), the Shandong Natural Science Foundation of China (Grant No. ZR2020ZD05) and the State Key Laboratory of Materials Processing and Die & Mould Technology, Huazhong University of Science and Technology (Grant No. P2022-013).

Disclosure statement

No potential conflict of interest was reported by the authors.

Data availability statement

The raw/processed data required to reproduce these findings cannot be shared at this time as the data also forms part of an ongoing study.

References

- [1] R. Tyagi, D.S. Xiong, J. Li, J. Dai, Elevated temperature tribological behavior of Ni based composites containing nano-silver and hBN, *Wear*. 269 (2010) 884–890. <https://doi.org/10.1016/j.wear.2010.08.022>.
- [2] N. Travitzky, P. Kumar, K.H. Sandhage, R. Janssen, N. Claussen, In-Situ Synthesis of Al₂O₃ Reinforced Ni-Based Composites, *Adv. Eng. Mater.* 5 (2003) 256–259. <https://doi.org/10.1002/adem.200300335>.
- [3] Z. Chen, P. Wei, S. Zhang, B. Lu, L. Zhang, X. Yang, K. Huang, Y. Huang, X. Li, Q. Zhao, Graphene reinforced nickel-based superalloy composites fabricated by additive manufacturing, *Mater. Sci. Eng. A*. 769 (2020) 138484. <https://doi.org/10.1016/j.msea.2019.138484>.
- [4] M.P. Behera, T. Dougherty, S. Singamneni, Conventional and Additive Manufacturing with Metal Matrix Composites: A Perspective, *Procedia Manuf.* 30 (2019) 159–166. <https://doi.org/10.1016/j.promfg.2019.02.023>.
- [5] J.P. Kruth, L. Froyen, J. Van Vaerenbergh, P. Mercelis, M. Rombouts, B. Lauwers, Selective laser melting of iron-based powder, in: *J. Mater. Process. Technol.*, 2004: pp. 616–622. <https://doi.org/10.1016/j.jmatprotec.2003.11.051>.

- [6] Q. Han, R. Setchi, S.L. Evans, Synthesis and characterisation of advanced ball-milled Al-Al₂O₃ nanocomposites for selective laser melting, *Powder Technol.* 297 (2016) 183–192. <https://doi.org/10.1016/j.powtec.2016.04.015>.
- [7] W.H. Yu, S.L. Sing, C.K. Chua, C.N. Kuo, X.L. Tian, Particle-reinforced metal matrix nanocomposites fabricated by selective laser melting: A state of the art review, *Prog. Mater. Sci.* 104 (2019) 330–379. <https://doi.org/10.1016/j.pmatsci.2019.04.006>.
- [8] C. Gao, Z. Wang, Z. Xiao, D. You, K. Wong, A.H. Akbarzadeh, Selective laser melting of TiN nanoparticle-reinforced AlSi10Mg composite: Microstructural, interfacial, and mechanical properties, *J. Mater. Process. Technol.* (2020). <https://doi.org/10.1016/j.jmatprotec.2020.116618>.
- [9] C. Han, R. Babicheva, J.D.Q. Chua, U. Ramamurty, S.B. Tor, C.N. Sun, K. Zhou, Microstructure and mechanical properties of (TiB+TiC)/Ti composites fabricated in situ via selective laser melting of Ti and B₄C powders, *Addit. Manuf.* (2020). <https://doi.org/10.1016/j.addma.2020.101466>.
- [10] Y. Yang, C. Lu, S. Peng, L. Shen, D. Wang, F. Qi, C. Shuai, Laser additive manufacturing of Mg-based composite with improved degradation behaviour, *Virtual Phys. Prototyp.* 15 (2020) 278–293. <https://doi.org/10.1080/17452759.2020.1748381>.
- [11] H. Zhang, D. Gu, C. Ma, M. Guo, J. Yang, H. Zhang, H. Chen, C. Li, K. Svynarenko, K. Kosiba, Understanding tensile and creep properties of WC reinforced nickel-based composites fabricated by selective laser melting, *Mater. Sci. Eng. A.* 802 (2021) 140431. <https://doi.org/10.1016/j.msea.2020.140431>.
- [12] Q. Han, Y. Gu, J. Huang, L. Wang, K.W.Q. Low, Q. Feng, Y. Yin, R. Setchi, Selective laser melting of Hastelloy X nanocomposite: Effects of TiC reinforcement on crack elimination and strength improvement, *Compos. Part B Eng.* 202 (2020) 108442. <https://doi.org/10.1016/j.compositesb.2020.108442>.
- [13] Q. Han, Y. Gu, L. Wang, Q. Feng, H. Gu, R. Johnston, R. Setchi, Effects of TiC content on microstructure and mechanical properties of nickel-based hastelloy X nanocomposites manufactured by selective laser melting, *Mater. Sci. Eng. A.* 796 (2020) 140008. <https://doi.org/10.1016/j.msea.2020.140008>.
- [14] S.A. Khairallah, A.T. Anderson, A. Rubenchik, W.E. King, Laser powder-bed fusion additive manufacturing: Physics of complex melt flow and formation mechanisms of pores, spatter, and denudation zones, *Acta Mater.* 108 (2016) 36–45.
- [15] M. Xia, D. Gu, G. Yu, D. Dai, H. Chen, Q. Shi, Selective laser melting 3D printing of Ni-based superalloy: understanding thermodynamic mechanisms, *Sci. Bull.* 61 (2016) 1013–1022. <https://doi.org/10.1007/s11434-016-1098-7>.
- [16] M.J. Matthews, G. Guss, S.A. Khairallah, A.M. Rubenchik, P.J. Depond, W.E. King, Denudation of metal powder layers in laser powder bed fusion processes, *Acta Mater.* 114 (2016) 33–42.
- [17] L.-X. Lu, N. Sridhar, Y.-W. Zhang, Phase field simulation of powder bed-based additive manufacturing, *Acta Mater.* 144 (2018) 801–809. <https://doi.org/10.1016/j.actamat.2017.11.033>.
- [18] V. Manvatkar, A. De, T. DebRoy, Heat transfer and material flow during laser assisted multi-layer additive manufacturing, *J. Appl. Phys.* 116 (2014) 124905. <https://doi.org/10.1063/1.4896751>.

- [19] M. Bayat, S. Mohanty, J.H. Hattel, Multiphysics modelling of lack-of-fusion voids formation and evolution in IN718 made by multi-track/multi-layer L-PBF, *Int. J. Heat Mass Transf.* 139 (2019) 95–114.
<https://doi.org/10.1016/j.ijheatmasstransfer.2019.05.003>.
- [20] T. Zhang, H. Li, S. Liu, S. Shen, H. Xie, W. Shi, G. Zhang, B. Shen, L. Chen, B. Xiao, M. Wei, Evolution of molten pool during selective laser melting of Ti–6Al–4V, *J. Phys. D. Appl. Phys.* 52 (2019) 055302. <https://doi.org/10.1088/1361-6463/aaee04>.
- [21] J. Shinjo, C. Panwisawas, Digital materials design by thermal-fluid science for multi-metal additive manufacturing, *Acta Mater.* 210 (2021) 116825.
<https://doi.org/10.1016/j.actamat.2021.116825>.
- [22] H. Gu, C. Wei, L. Li, Q. Han, R. Setchi, M. Ryan, Q. Li, Multi-physics modelling of molten pool development and track formation in multi-track, multi-layer and multi-material selective laser melting, *Int. J. Heat Mass Transf.* 151 (2020) 119458.
<https://doi.org/10.1016/j.ijheatmasstransfer.2020.119458>.
- [23] Y. Yang, C. Doñate-Buendía, T.D. Oyedepi, B. Gökce, B.-X. Xu, Nanoparticle Tracing during Laser Powder Bed Fusion of Oxide Dispersion Strengthened Steels, *Materials (Basel)*. 14 (2021) 3463. <https://doi.org/10.3390/ma14133463>.
- [24] A. Matsunawa, V. Semak, The simulation of front keyhole wall dynamics during laser welding, *J. Phys. D. Appl. Phys.* (1997). <https://doi.org/10.1088/0022-3727/30/5/013>.
- [25] M. Courtois, M. Carin, P. Le Masson, S. Gaied, M. Balabane, A complete model of keyhole and melt pool dynamics to analyze instabilities and collapse during laser welding, *J. Laser Appl.* 26 (2014) 042001. <https://doi.org/10.2351/1.4886835>.
- [26] A. Hussein, L. Hao, C. Yan, R. Everson, Finite element simulation of the temperature and stress fields in single layers built without-support in selective laser melting, *Mater. Des.* 52 (2013) 638–647. <https://doi.org/10.1016/j.matdes.2013.05.070>.
- [27] S. Anisimov, V. Khokhlov, *Instabilities in laser matter interaction*, CRC press, 1995.
- [28] A.J.C. Ladd, R. Verberg, Lattice-Boltzmann simulations of particle-fluid suspensions, *J. Stat. Phys.* (2001). <https://doi.org/10.1023/A:1010414013942>.
- [29] R. Glowinski, T.-W. Pan, T.I. Hesla, D.D. Joseph, A distributed Lagrange multiplier/fictitious domain method for particulate flows, *Int. J. Multiph. Flow.* 25 (1999) 755–794. [https://doi.org/10.1016/S0301-9322\(98\)00048-2](https://doi.org/10.1016/S0301-9322(98)00048-2).
- [30] S.A. Hosseini, H. Vahedi Tafreshi, Modeling particle-loaded single fiber efficiency and fiber drag using ANSYS-Fluent CFD code, *Comput. Fluids.* (2012).
<https://doi.org/10.1016/j.compfluid.2012.06.017>.
- [31] A. Li, G. Ahmadi, Dispersion and Deposition of Spherical Particles from Point Sources in a Turbulent Channel Flow, *Aerosol Sci. Technol.* 16 (1992) 209–226.
<https://doi.org/10.1080/02786829208959550>.
- [32] Y.S. Lee, W. Zhang, Modeling of heat transfer, fluid flow and solidification microstructure of nickel-base superalloy fabricated by laser powder bed fusion, *Addit. Manuf.* 12 (2016) 178–188. <https://doi.org/10.1016/j.addma.2016.05.003>.
- [33] H. Gu, C. Wei, L. Li, Q. Han, R. Setchi, M. Ryan, Q. Li, Multi-physics modelling of molten pool development and track formation in multi-track, multi-layer and multi-material selective laser melting, *Int. J. Heat Mass Transf.* (2020).
<https://doi.org/10.1016/j.ijheatmasstransfer.2020.119458>.

- [34] J.L. Tan, C. Tang, C.H. Wong, Study and modeling of melt pool evolution in selective laser melting process of SS316L, *MRS Commun.* (2018). <https://doi.org/10.1557/mrc.2018.180>.
- [35] Q. Han, Y. Gu, L. Wang, Q. Feng, H. Gu, R. Johnston, R. Setchi, Effects of TiC content on microstructure and mechanical properties of nickel-based hastelloy X nanocomposites manufactured by selective laser melting, *Mater. Sci. Eng. A.* 796 (2020) 140008. <https://doi.org/10.1016/j.msea.2020.140008>.
- [36] Q. Han, Y. Gu, R. Setchi, F. Lacan, R. Johnston, S.L. Evans, S. Yang, Additive manufacturing of high-strength crack-free Ni-based Hastelloy X superalloy, *Addit. Manuf.* 30 (2019) 100919. <https://doi.org/10.1016/j.addma.2019.100919>.
- [37] Y.-C. Wu, C.-H. San, C.-H. Chang, H.-J. Lin, R. Marwan, S. Baba, W.-S. Hwang, Numerical modeling of melt-pool behavior in selective laser melting with random powder distribution and experimental validation, *J. Mater. Process. Technol.* 254 (2018) 72–78. <https://doi.org/10.1016/j.jmatprotec.2017.11.032>.
- [38] Q. Guo, C. Zhao, L.I. Escano, Z. Young, L. Xiong, K. Fezzaa, W. Everhart, B. Brown, T. Sun, L. Chen, Transient dynamics of powder spattering in laser powder bed fusion additive manufacturing process revealed by in-situ high-speed high-energy x-ray imaging, *Acta Mater.* 151 (2018) 169–180. <https://doi.org/10.1016/j.actamat.2018.03.036>.
- [39] T.-N. Le, Y.-L. Lo, Effects of sulfur concentration and Marangoni convection on melt-pool formation in transition mode of selective laser melting process, *Mater. Des.* 179 (2019) 107866. <https://doi.org/10.1016/j.matdes.2019.107866>.
- [40] D. Zhang, P. Zhang, Z. Liu, Z. Feng, C. Wang, Y. Guo, Thermofluid field of molten pool and its effects during selective laser melting (SLM) of Inconel 718 alloy, *Addit. Manuf.* 21 (2018) 567–578. <https://doi.org/10.1016/j.addma.2018.03.031>.
- [41] Q. Chen, G. Guillemot, C.-A. Gandin, M. Bellet, Numerical modelling of the impact of energy distribution and Marangoni surface tension on track shape in selective laser melting of ceramic material, *Addit. Manuf.* 21 (2018) 713–723. <https://doi.org/10.1016/j.addma.2018.03.003>.
- [42] Y. Liu, J. Zhang, Z. Pang, Numerical and experimental investigation into the subsequent thermal cycling during selective laser melting of multi-layer 316L stainless steel, *Opt. Laser Technol.* 98 (2018) 23–32. <https://doi.org/10.1016/j.optlastec.2017.07.034>.
- [43] Z. Gan, H. Liu, S. Li, X. He, G. Yu, Modeling of thermal behavior and mass transport in multi-layer laser additive manufacturing of Ni-based alloy on cast iron, *Int. J. Heat Mass Transf.* 111 (2017) 709–722. <https://doi.org/10.1016/j.ijheatmasstransfer.2017.04.055>.